

Accelerating the analysis of optical quantum systems using the Koopman operator

Anna Hunstig¹, Sebastian Peitz¹, Hendrik Rose² and Torsten Meier³

Abstract—The prediction of photon echoes is a crucial technique for gaining an understanding of optical quantum systems. However, it requires a large number of simulations with varying parameters and/or input pulses, which renders numerical studies expensive. This article investigates how we can use data-driven surrogate models based on the Koopman operator to accelerate this process while maintaining accuracy over a large number of time steps. To this end, we employ a bilinear Koopman model using extended dynamic mode decomposition and simulate the optical Bloch equations for an ensemble of inhomogeneously broadened two-level systems. Such systems are well suited to describe the excitation of excitonic resonances in semiconductor nanostructures, for example, ensembles of semiconductor quantum dots. We perform a detailed study on the required number of system simulations such that the resulting data-driven Koopman model is sufficiently accurate for a wide range of parameter settings. We analyze the L2 error and the relative error of the photon echo peak and investigate how the control positions relate to the stabilization. After proper training, our methods can predict the quantum ensemble’s dynamics accurately and numerically efficiently.

I. INTRODUCTION

Linearization of nonlinear dynamical systems is a goal in many research areas, ranging from fluid dynamics [1] over climate models [2] to robotics [3]. The Koopman operator, originally introduced by Koopman in 1931 [4], is a linear operator on the space of observables of the system. It not only allows for a linear representation of nonlinear dynamics but also entails global geometric properties via its eigendecomposition [5], [6]. Various computational methods have been established to date, dynamic mode decomposition (DMD) [7], [8], [9], [10] and its generalization extended dynamic mode decomposition (EDMD) [11], [12] being two of the most popular methods. While the Koopman operator has been well-researched in general and also for particular system classes such as measure-preserving or control systems [13], [14], [15], its application in quantum physics is fairly new. Some recent investigations include [16] and [17]. Quantum-mechanical descriptions of complex systems are usually computationally challenging and numerically expensive. We examine how a Koopman operator-based model can serve as a surrogate model to conduct parameter studies on quantum systems more efficiently.

¹Anna Hunstig and Sebastian Peitz are with the Department of Computer Science, Paderborn University, Germany hunstiga@mail.upb.de, sebastian.peitz@upb.de

²Hendrik Rose is with the Institute for Photonic Quantum Systems (PhoQS), Paderborn University, Germany hendrik.rose@upb.de

³Torsten Meier is with the Department of Physics and Institute for Photonic Quantum Systems (PhoQS), Paderborn University, Germany torsten.meier@upb.de

The quantum system we consider in this work is an inhomogeneously broadened ensemble of two-level systems (TLS) which describe, e.g. excitonic resonances in semiconductor quantum dots (QD). These systems are known to emit electromagnetic radiation in the form of photon echoes in four-wave-mixing schemes which involve impulsive excitation with two time-delayed optical pulses that entail non-linear dynamics, see [18], [19]. Photon echoes have been proposed as a key ingredient for realizing quantum memory protocols [20] and it was shown recently that the emission time of photon echoes can be controlled optically [21], [22]. When an excitonic resonance of an inhomogeneously broadened ensemble of quantum dots, called quantum ensemble (QE), is excited by a short optical laser pulse at $t = 0$, the macroscopic polarization, i.e., the sum over all individual microscopic optical polarizations, of the QE dephases. Dephasing is the rapid decay with time on a duration which is inversely proportional to the width of the distribution of transition frequencies. This dephasing can be reversed by exciting the ensemble with a second temporally delayed laser pulse at $t = \tau$. The phase conjugation induced by the second pulse leads to rephasing of the microscopic polarizations which results in the buildup of a macroscopic polarization at $t = 2\tau$. This transient macroscopic polarization is the source for the emission of a pulse of electromagnetic radiation which is known as the photon echo. The contribution of this paper is to demonstrate the advantage of Koopman theory and a data-driven approximation algorithm like DMD over regular procedures in efficiency for predicting optical quantum experiments accurately over a long timescale.

II. PRELIMINARIES

A. Quantum physical model

The optical properties and dynamics of near-resonantly excited TLS are obtained by solving the optical Bloch equations (OBE) in the rotating-wave approximation (RWA) [18]. The OBE describe the dynamics of electronic excitations driven by optical fields. They can be formulated in terms of the occupation probability n_l of the energetically higher level and the microscopic polarization or coherence p_l between the two levels for the l -th TLS, respectively. In the absence of losses they read:

$$\begin{bmatrix} \dot{p}_l(t) \\ \dot{n}_l(t) \end{bmatrix} = \begin{bmatrix} -i\delta_l p_l(t) + i\Omega_R(t)(1 - 2n_l(t)) \\ 2\Omega_R(t)\Im(p_l(t)) \end{bmatrix}. \quad (1)$$

We denote time in picoseconds and frequency in inverse picoseconds. Besides the two-dimensional complex state $\mathbf{x}(t) = (p_l(t), n_l(t))$, the OBE depend on two additional

entities: the Rabi frequency $\Omega_R(t) = dE(t)/\hbar$, proportionate to the electric field $E(t)$ by the dipole matrix element d and the reduced Planck constant \hbar , and the optical detuning $\delta_l = \omega_l - \omega_L$, which is given by the difference between the transition frequency of the l -th TLS ω_l and the laser frequency ω_L . We are interested in the macroscopic polarization $P(t)$ of the QE, which can be calculated as the weighted sum of microscopic polarizations

$$P(t) := \sum_{l=1}^N \sigma(\delta_l) p_l(t) \quad (2)$$

with N denoting the size of the QE, i.e. the number of considered TLS. Note that $P(t)$ is a dimensionless quantity and the physical polarization can be obtained by multiplying with d . The σ in (2) denotes the weight distribution of the detunings and is characterized by its full width at half maximum (FWHM), corresponding to the inhomogeneous broadening of the transition frequencies. For a discrete set of detunings \mathcal{D} we use the Gaussian distribution $\sigma : \mathcal{D} \rightarrow \mathbb{R}$

$$\sigma(\delta_l) = \exp \left\{ -\frac{1}{2} \left(\frac{2\sqrt{2 \ln 2} \hbar \delta_l}{\text{FWHM}} \right)^2 \right\}. \quad (3)$$

The set of detunings will always take the form of a linearly spaced, discrete array $\mathcal{D} = [-R, \dots, R] \frac{\text{meV}}{\hbar}$ with R referred to as “range”. The judicious selection of hyperparameters R and FWHM ensures that the physical experiment is modeled adequately and all emerging physical dynamics can be observed numerically, if the machine-learning model is sophisticated enough. A possible negligence case is choosing R too small compared to FWHM, leading to the domain of σ not being a subset of \mathcal{D} and thereby σ not being completely represented. However, for the duration of the pulses utilized in our experiments, the relevant dynamics, i.e. detuning responses with large amplitudes, occur within a narrower detuning range than what would be represented by a range that encompasses σ entirely. Consequently, a broader range could lead to lower resolution of these critical detunings.

The discretization of frequencies causes unphysical repetitions in the polarization after the photon echo. The time of these repetitions, called “revival time”, depends on the emission times and frequencies of the laser pulses and the weight distribution. For the pulses used in [21] and simulated in section IV-A it can be calculated apriori via

$$T_{\text{Rev}} = \hbar \frac{2\pi(N-1)}{2R \cdot 1\text{meV}}, \quad (4)$$

which evaluates to $T_{\text{Rev}} = 110.1$ for $N = 800$ and $R = 15$.

B. The Koopman operator

We consider a continuous-time control system

$$\dot{\mathbf{x}}(t) = f(\mathbf{x}(t), \mathbf{u}(t)) \quad (5)$$

with real-valued states $\mathbf{x}(t) \in \mathcal{X} \subseteq \mathbb{R}^d$ and control $\mathbf{u}(t) \in \mathcal{U} \subseteq \mathbb{R}^p$. The dynamics are described by the right-hand side $f : \mathcal{X} \times \mathcal{U} \rightarrow \mathbb{R}^d$. Let $\mathbf{u}(t) = \mathbf{u}$ be constant. We

can equivalently describe the dynamics by

$$\mathbf{x}(t + \Delta t) = \Phi_{\mathbf{u}}^{\Delta t}(\mathbf{x}(t)), \quad (6)$$

where $\Phi_{\mathbf{u}}^{\Delta t} : \mathcal{X} \rightarrow \mathcal{X}$ is the flow map with input \mathbf{u} . Whereas in general no linearity assumptions can be made about $\Phi_{\mathbf{u}}^{\Delta t}$, the finite-time Koopman operator gives a linear description of (6) by mapping observables instead of the system states \mathbf{x} . Let \mathcal{S} be a space of L^2 -functions on \mathcal{X} that is closed under composition with the flow map. Then the family $(\mathcal{K}_{\mathbf{u}}^{\Delta t})_{\Delta t \geq 0}$ of Koopman operators on \mathcal{S} is defined by

$$\mathcal{K}_{\mathbf{u}}^{\Delta t} \psi := \psi \circ \Phi_{\mathbf{u}}^{\Delta t}, \quad \psi \in \mathcal{S}. \quad (7)$$

The Koopman family is a semigroup if $(\Phi_{\mathbf{u}}^{\Delta t})_{\Delta t \geq 0}$ is a semigroup, see [23]. The generator of the semigroup [24] gives an analogous description for (5) by

$$\mathcal{K}_{\mathbf{u}} \psi := \lim_{\Delta t \rightarrow 0} \frac{\mathcal{K}_{\mathbf{u}}^{\Delta t} \psi - \psi}{\Delta t}, \quad (8)$$

for all $\psi \in \mathcal{S}$ such that this limit exists. Inserting (7) into (8) and recalling the definition of the first derivative one obtains

$$\mathcal{K}_{\mathbf{u}} \psi(\mathbf{x}(t)) = \frac{d}{dt} \psi(\mathbf{x}(t)) = \dot{\mathbf{x}}(t) \cdot \nabla_{\mathbf{x}} \psi(\mathbf{x}(t)),$$

which yields

$$\mathcal{K}_{\mathbf{u}} \psi = f \cdot \nabla_{\mathbf{x}} \psi. \quad (9)$$

Hence, the Koopman generator $\mathcal{K}_{\mathbf{u}}$ differentiates observables wrt. the dynamics, whereas the finite-time operators $\mathcal{K}_{\mathbf{u}}^{\Delta t}$ evolve observables one time step forward. To approximate the Koopman operator, conventionally a set of functions $\Psi = \{\psi_1, \dots, \psi_z\}$ like eigenfunctions or generic basis functions such as polynomials or radial basis functions is chosen to generate the function space $\mathcal{S} = \text{span}(\psi_1, \dots, \psi_z)$.

1) *Control-affine systems:* Suppose the system in (5) is control-affine and we again actuate with a fixed, constant $\mathbf{u} \in \mathbb{R}^p$

$$\dot{\mathbf{x}}(t) = f(\mathbf{x}(t), \mathbf{u}) = g(\mathbf{x}(t)) + \sum_{j=1}^p u^j(t) h_j(\mathbf{x}(t)), \quad (10)$$

where $g : \mathcal{X} \rightarrow \mathcal{X}$, $h_j : \mathcal{X} \rightarrow \mathcal{X}$ may be non-linear and $u^j \in \mathbb{R}$ denotes the j -th coordinate of the vector \mathbf{u} . Now, the Koopman ansatz is especially convenient because the control affinity of (10) translates to the Koopman generator, resulting in a bilinear model. This will be the main idea for the algorithms in section III and is based on the observations in [25]. To see this, one recognizes that the Koopman generator for the system (10) is given by $\mathcal{K}_{\mathbf{u}} \psi = g \cdot \nabla_{\mathbf{x}} \psi + \sum_{j=1}^p u^j h_j \cdot \nabla_{\mathbf{x}} \psi$, compare Eq. (9). When using a linear combination of q constant controls $\mathbf{u}_1, \dots, \mathbf{u}_q$ with $\mathbf{u} = \sum_{i=1}^q \alpha_i \mathbf{u}_i$ and $\alpha_i \in \mathbb{R}$ this becomes

$$\begin{aligned} \mathcal{K}_{\mathbf{u}} \psi &= g \cdot \nabla_{\mathbf{x}} \psi + \sum_{j=1}^p \sum_{i=1}^q \alpha_i u_i^j h_j \cdot \nabla_{\mathbf{x}} \psi \\ &= \mathcal{K}_0 \psi + \sum_{i=1}^q \alpha_i \sum_{j=1}^p u_i^j h_j \cdot \nabla_{\mathbf{x}} \psi, \end{aligned} \quad (11)$$

where we rearranged the sum and used that $\mathcal{K}_0\psi = g \cdot \nabla_{\mathbf{x}}\psi$ is the case of the unactuated system. By defining $\mathcal{B}_{\mathbf{u}} := \mathcal{K}_{\mathbf{u}} - \mathcal{K}_0$ we obtain $\mathcal{B}_{\mathbf{u}_i}\psi = \sum_{j=1}^p u_i^j h_j \cdot \nabla_{\mathbf{x}}\psi$ and (11) can be expressed as

$$\mathcal{K}_{\mathbf{u}}\psi = \left(\mathcal{K}_0 + \sum_{i=1}^q \alpha_i \mathcal{B}_{\mathbf{u}_i} \right) \psi. \quad (12)$$

We now select $q = p$ and $\mathbf{u}_i = \mathbf{e}_i$ as the standard p -dimensional unit vectors and $\alpha_i = u^i$ to specify the i -th component of \mathbf{u} , i.e. $\mathbf{u} = \sum_{i=1}^p u^i \mathbf{e}_i$. We receive the following system, which is often called bilinear in literature, meaning linear in the observed space $\psi(\mathbf{x}(t))$ and affine-linear in the control,

$$\mathcal{K}_{\mathbf{u}}\psi(\mathbf{x}(t)) = \left(\mathcal{K}_0 + \sum_{i=1}^p u^i \mathcal{B}_{\mathbf{e}_i} \right) \psi(\mathbf{x}(t)) \quad (13)$$

to represent the previously non-linear system (10). This bilinear model can be generalized to time-dependent control inputs by leveraging time-dependent coefficients in the control representation and acknowledging that linearity is preserved. The system wrt. control $\mathbf{u}(t) = \sum_{i=1}^p u^i(t) \mathbf{e}_i$ takes the form $\mathcal{K}_{\mathbf{u}(t)}\psi(\mathbf{x}(t)) = (\mathcal{K}_0 + \sum_{i=1}^p u^i(t) \mathcal{B}_{\mathbf{e}_i}) \psi(\mathbf{x}(t))$. Note that, all previous models employed the Koopman generator. The finite-time operators $\mathcal{K}_{\mathbf{u}}^{\Delta t}$ establish a similar system to (15) and can also be generalized to time-dependent control in the same manner as above. They are not control-affine but control-affine up to first order in Δt , i.e.

$$\mathcal{K}_{\mathbf{u}(t)}^{\Delta t} = \mathcal{K}_0^{\Delta t} + \sum_{i=1}^p u^i(t) \mathcal{B}_{\mathbf{e}_i}^{\Delta t} + \mathcal{O}(\Delta t^2). \quad (14)$$

See [25] for a proof. While this approach tends to be more efficient because integration in time can be omitted, the first-order error occurs even if the underlying system is bilinear, as in the case of the OBE.

III. ALGORITHMS

We propose two algorithms based on [25] and Eq. (15), that construct a bilinear Koopman model for control-affine systems using EDMD. We will refer to the method in [25] as bilinear EDMDc. DMD [8] has become a popular technique to approximate the Koopman generator because it is purely data-driven and computationally efficient even for high-dimensional data. To approximate the Koopman operator, linear observations of the state space are collected instead of system states. The relaxation of linear observables leads to EDMD [11] and also the constraint for evenly spaced time points can be relaxed. Other methods based on (E)DMD for control systems can be found, for example, in [26] and [12]. Bilinear EDMDc coincides with other EDMD methods in that the Koopman generators are approximated on the space of observables spanned by an a priori fixed set of nonlinear basis functions Ψ , called dictionary. The distinguishing idea is to compute Koopman operator approximations individually wrt. different fixed actuations and constructing a bilinear model (15) by interpolating these generators wrt. the target actuation. Note that the OBE (1) establish a bilinear system

themselves, thus direct linearization would in principle be possible, i.e. the Koopman generators could be computed exactly. Nonetheless, the following algorithms use the finite-time operator approach (14), which induces an error even on bilinear systems, but has the advantage of easier generalization to a broad class of nonlinear systems where the underlying dynamics may not be given explicitly.

We first introduce the general bilinear EDMDc algorithm in III-A with the universal representation of the actuation $\mathbf{u} = \sum_{i=1}^c \alpha^i \mathbf{u}_i$ by basis controls \mathbf{u}_i that are not necessarily the standard unit-vectors and $c \neq p$, compare to (12). Our first application, BE, uses the representation via unit control vectors as stated in (14). Lastly, the amendment BERG, entails both representations. For all algorithms, we denote the set of training control vectors by \mathbf{U} and define $c := |\mathbf{U}|$. The total number of distinct control points is $c + 1$ as the zero-control $\mathbf{0}$ is always needed. We assume $\mathbf{0} \notin \mathbf{U}$ to avoid redundancy. The number z denotes the number of dictionary functions $|\Psi|$, thereby equal to the dimension of the lifted state vector $\Psi(\mathbf{x}(t))$. The approximations of the operators $\mathcal{K}_{\mathbf{u}}^{\Delta t}$ are the matrices $\mathbf{K}_{\mathbf{u}}^{\Delta t}$.

A. Bilinear EDMDc

The *training* of bilinear EDMDc works as follows:

- 1) Fix dictionary Ψ , control points \mathbf{U} and time step Δt for integration.
- 2) Collect initial system states $\mathbf{x}_k := \mathbf{x}(t_k)$ in a matrix \mathbf{X} and lift \mathbf{X} to

$$\Psi(\mathbf{X}) = \begin{bmatrix} | & & | \\ \Psi(\mathbf{x}_1) & \dots & \Psi(\mathbf{x}_n) \\ | & & | \end{bmatrix} \in \mathbb{R}^{z \times n}.$$

- 3) Calculate $\mathbf{G} := (\Psi(\mathbf{X})\Psi(\mathbf{X})^\top)^\dagger$.
- 4) For every control $\mathbf{u} \in \mathbf{U}$ and for $\mathbf{u} = \mathbf{0}$:
 - a) Generate the propagated system states $\mathbf{x}'_{\mathbf{u},k} := \Phi_{\mathbf{u}}^{\Delta t}(\mathbf{x}_k)$ and build matrices $\mathbf{X}'_{\mathbf{u}}$.
 - b) Calculate $\mathbf{A}_{\mathbf{u}} := \Psi(\mathbf{X})\Psi(\mathbf{X}'_{\mathbf{u}})^\top$.
 - c) Approximate the Koopman operator $\mathbf{K}_{\mathbf{u}}^{\Delta t} = (\mathbf{G}\mathbf{A}_{\mathbf{u}})^\top$.

Prediction entails the following steps:

- 1) For every test timestep t_k represent the test actuation $\mathbf{u}(t_k) = \sum_{i=1}^c \alpha_i(t_k) \mathbf{u}_i$, as a linear combination of the trained control vectors $\mathbf{u}_i \in \mathbf{U}$.
- 2) Compute the respective Koopman matrix as a linear combination of the learned matrices $\mathbf{K}_{\mathbf{u}(t_k)}^{\Delta t} = \mathbf{K}_0^{\Delta t} + \sum_{i=1}^c \alpha_i(t_k) \mathbf{B}_{\mathbf{u}_i}^{\Delta t}$.
- 3) Multiply Koopman matrices with the columns of matrix $\Psi(\mathbf{X})$ to approximate the system at timestep t_k wrt. control $\mathbf{u}(t_k)$ via $\mathbf{K}_{\mathbf{u}(t_k)}^{\Delta t} \Psi(\mathbf{x}_k) \approx \Phi_{\mathbf{u}(t_k)}^{\Delta t}(\Psi(\mathbf{x}_k))$.

B. BE and BERG

To fit bilinear EDMDc to the simulation of the OBE, we note that (1) is affine-linear in the system state, implying that the choice of Ψ as the set of monomials up to order 1 is sufficient. Framed differently, we add a bias term in contrast to standard DMD. Since the system state in the OBE

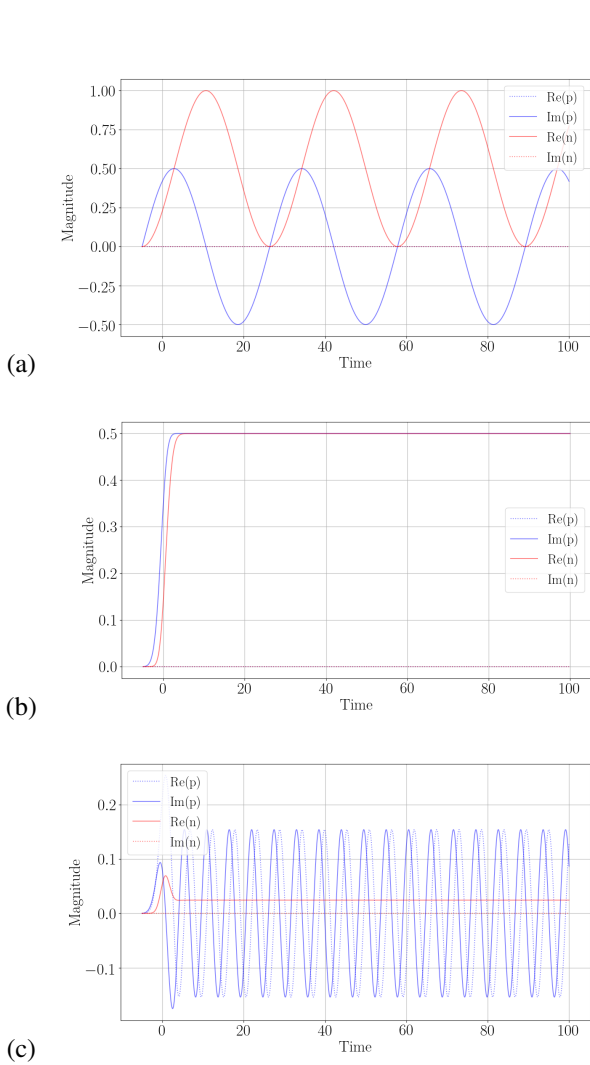


Fig. 1: Solutions of the OBE wrt. different laser pulses and detunings. (a) Constant pulse with amplitude 0.2, i.e., $\Omega_R(t) = \frac{1}{5} \Theta(t)$, where Θ is the Heaviside function, and detuning $\delta = 0$. (b), (c) Gaussian pulse with area $\frac{\pi}{2}$ and duration 2.5. Detunings $\delta = 0$ and $\delta = 0.75 \frac{\text{meV}}{\hbar}$, respectively.

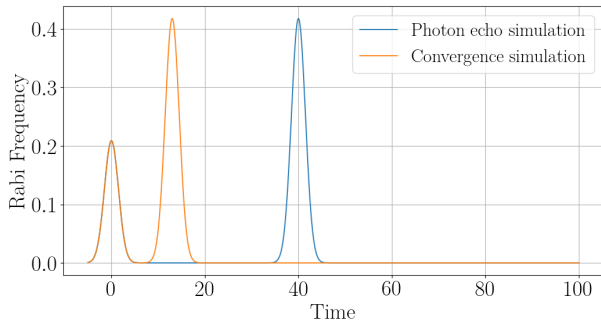


Fig. 2: The optical pulses used in the experiments. Photon echo: Section IV-A, Convergence: Section IV-B.

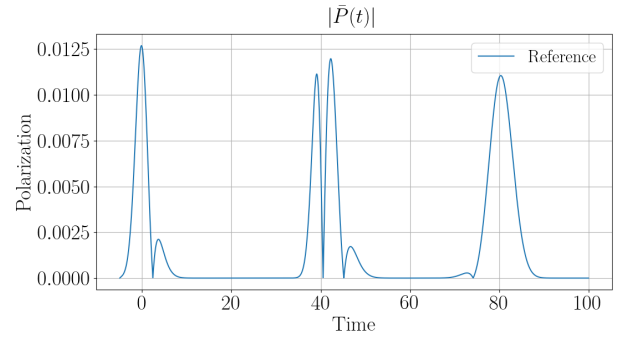


Fig. 3: The polarization in the photon echo experiment. The echo occurs at $t = 80$.

is a two-dimensional complex vector, we split both p and n into real and imaginary parts and obtain a four-dimensional real vector, coinciding with the theory from section II-B assuming real values. Besides the system state, the OBE entail the Rabi frequency $\Omega_R(t) \in \mathbb{R}$ as a time-dependent control parameter and the detuning $\delta \in \mathbb{R}$ as a constant parameter. The difficulty in producing an accurate model for the OBE lies in capturing the dynamics for the entire quantum ensemble, consisting of TLS with varying δ , excited by a laser pulse with varying $\Omega_R(t)$. Fig. 1 exemplifies how varying $\Omega_R(t)$ and δ create noticeably different dynamics. We aim to learn a bilinear model wrt. the two-dimensional control $u(t) = [\Omega_R(t), \delta]$. Let Ω and \mathbf{D} be the discretized grid of training points for Ω_R and δ respectively. We denote $m := |\mathbf{D}|$. The training control set is $\mathbf{U} = \Omega \times \mathbf{D}$ and both accuracy, as well as computational efficiency of the resulting model, are ultimately determined by the refinement of \mathbf{U} and the step size for time. BE and BERG share that $n = 100$ random initial system states $\mathbf{x}_k \in [-1, 1]^4$ were constructed for training and the OBE were solved with the same Runge-Kutta method of order four and time step Δt .

1) *Bilinear EDMDc (BE)*: We use the standard unit vectors $\mathbf{U} = \{[1, 0], [0, 1]\}$, $c = 2$ as control points. Note that linear combinations of the unit vectors like $[1, 1]$ are not necessary since we can construct the corresponding Koopman operator as a linear combination of the Koopman operators wrt. \mathbf{U} . Similarly, $\mathbf{u}(t_k) = \Omega_R(t_k) [1, 0] + \delta [0, 1]$ implies that the prediction at time point t_k is given by

$$\mathbf{K}_{\mathbf{u}(t_k)}^{\Delta t} \mathbf{x}_k = \left(\mathbf{K}_{[0,0]}^{\Delta t} + \Omega_R(t_k) \mathbf{B}_{[1,0]}^{\Delta t} + \delta \mathbf{B}_{[0,1]}^{\Delta t} \right) \mathbf{x}_k, \quad (15)$$

see (14). Section IV-A shows that this model is not stable for the range and pulse used in the photon echo experiment due to the inaccuracies introduced by the first-order error from the finite-time operators. Prediction with BE on different hyperparameter settings suggested that it was in particular the rapid fluctuations in the dynamics of the OBE caused by varying the range R . This motivated the introduction of additional control points.

2) *BE on refined grid (BERG)*: We maintain $\Omega = \{0, 1\}$, but refine \mathbf{D} to consist of m values between $-R$ and R . That is, \mathbf{D} is a coarser instantiation of the test detunings \mathcal{D} . In contrast to the single, global BE model (15) we

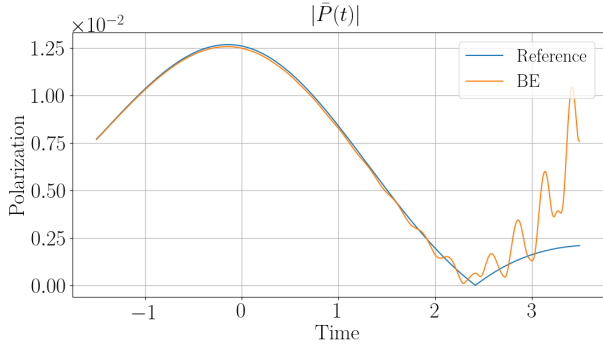


Fig. 4: BE in the photon echo simulation with step size $\Delta t = 0.01$.

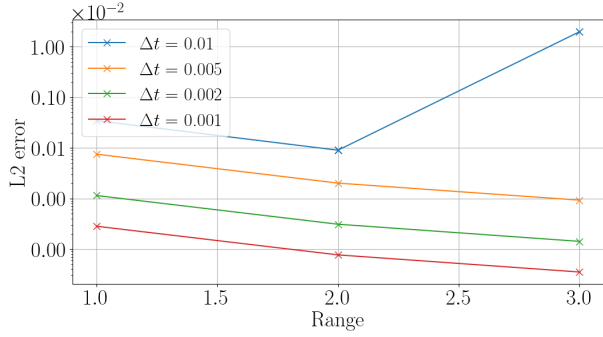


Fig. 5: L2 error of BE against the detuning range and for different step sizes.

now construct a family of bilinear models parameterized by \mathbf{D} , where each model interpolates between two $\delta_1, \delta_2 \in \mathbf{D}$ closest to the corresponding test detuning. Consider a fixed test control $u_i = [\omega_i, \delta_i]$ and let $\delta_1, \delta_2 \in \mathbf{D}$ be the two training detunings that are closest to δ_i wrt. Euclidean distance. Then $\delta_i = (1-a)\delta_1 + a\delta_2$ for some $a \in [0, 1]$ and $[\omega_i, \delta_i] = \omega_i [1, 0] + (1-a) [0, \delta_1] + a [0, \delta_2]$. Thereby,

$$\begin{aligned} \mathbf{K}_{[\omega_i, \delta_i]}^{\Delta t} \mathbf{x}_k &= \mathbf{K}_{[0,0]}^{\Delta t} \mathbf{x}_k + \omega_i \mathbf{B}_{[1,0]}^{\Delta t} \mathbf{x}_k \\ &\quad + (1-a) \mathbf{B}_{[0,\delta_1]}^{\Delta t} \mathbf{x}_k + a \mathbf{B}_{[0,\delta_2]}^{\Delta t} \mathbf{x}_k \\ &= \left(\mathbf{K}_{[0,0]}^{\Delta t} + \omega_i \mathbf{B}_{[1,0]}^{\Delta t} + \mathbf{B}_{[0,\delta]}^{\Delta t} \right) \mathbf{x}_k, \end{aligned}$$

where we abbreviated $\mathbf{B}_{[0,\delta]}^{\Delta t} := (1-a) \mathbf{B}_{[0,\delta_1]}^{\Delta t} + a \mathbf{B}_{[0,\delta_2]}^{\Delta t}$.

IV. RESULTS

A. The photon echo

Our ultimate goal is to learn a model that accurately simulates the dynamics of the OBE in the photon echo experiment as demonstrated in [21]. In this setting, the QE consists of $N = 800$ TLS with evenly spaced detunings in the range $R = 15$ and a weight distribution σ defined by FWHM = 7.5 meV. The exciting signal is composed of two pulses, each with duration 2.5. The initial pulse has pulse area $\frac{\pi}{2}$ and is centered at $t = 0$, the second is a π -pulse, centered at $t = 40$. A plot can be found in Fig. 2. The reference data is computed with the initial value solver

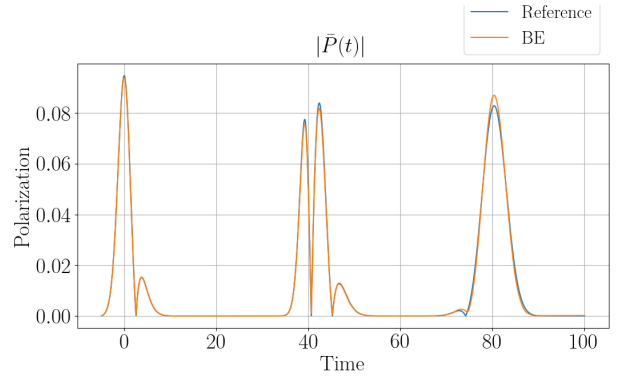


Fig. 6: BE in the modified photon echo simulation with range $R = 2$ and step size $\Delta t = 0.01$.

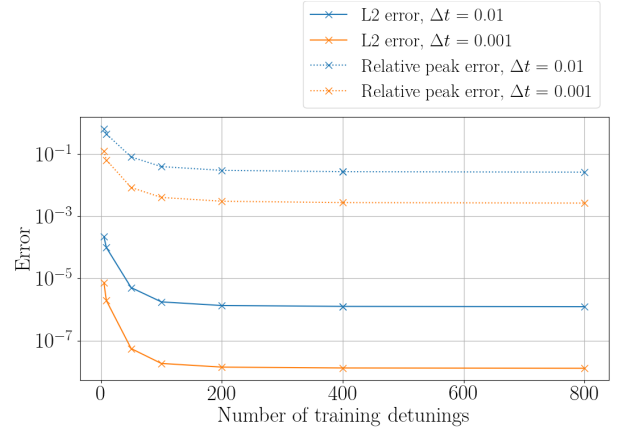


Fig. 7: L2 error and relative peak error of BERG in the photon echo simulation for different step sizes.

from SciPy [27], using RK45 and parameters $\Delta t = 0.01$, $\text{rtol} = 1e-8$ and $\text{atol} = 1e-11$ for the interpolation, see Fig. 3 for a visualization of the polarization as calculated by Eq. (2). Evaluation occurs from $t = -5$ to $t = 100$, and we select two error measures that remain invariant under the size of the ensemble N , as this variable will vary in simulation two (Section IV-B). We aim to quantify both the overall error as well as the deviation of the model in the photon echo peak. Let $\bar{P}(t) = \frac{P(t)}{N}$ be the normalized polarization, then the respective L2 error is given by

$$L_2(\bar{P}_{Ref}, \bar{P}_{BE}) = \int_{t=-5}^{t=100} \left(\frac{P_{Ref}(t)}{N} - \frac{P_{BE}(t)}{N} \right)^2 dt,$$

where P_R and P_{BE} denote the macroscopic polarization of the reference and BE, respectively. We write S_{Ref} and S_{BE} for the photon echo peak of the reference and BE and consider the relative peak error

$$L_{peak}(P_{Ref}, P_{BE}) = \left| \frac{S_{Ref} - S_{BE}}{S_{Ref}} \right|.$$

When simulating the photon echo experiment with BE and a step size of $\Delta t = 0.01$, the model quickly deviates from the reference calculation, see Fig. 4. Although the reduction of the step size to $\Delta t = 0.001$ slightly decreases the L2 error,

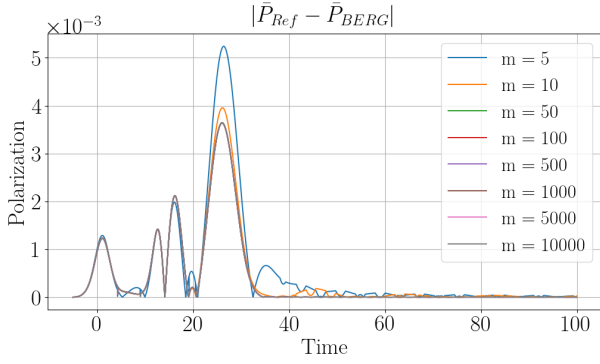


Fig. 8: Difference between normalized polarization of reference and BERG in the second simulation.

BE does not suffice to model the original experiment. We observe that the L2 error of the model heavily depends on the detuning range that is used, see Fig. 5. Note that a range $R \neq 15$ is not consistent with the original experiment. For $\Delta t = 0.01$ the lowest L2 error is of magnitude 10^{-5} and attained at $R = 2$. With these parameters BE matches the reference trajectory and approaches the correct photon echo peak, which is supported by a relative peak error of 0.05, see Fig. 6. However, for greater ranges $R \geq 4$, the L2 error diverges. BE is therefore not relevant for the prediction of the OBE in general. We find that, although the underlying dynamics are comparatively simple, the large number of time steps, in combination with the control input, poses substantial challenges. This implies that the modeling process needs to be performed judiciously.

In BERG, the refinement of training detunings \mathbf{D} , i.e. increasing m , decreases the error caused by interpolating the operators. The trade-off between m and the error measures is illustrated in Fig. 7. The trajectories for the two error measures exhibit similarity, leading to two conclusions. Firstly, it is evident that the step size significantly influences errors. Second, $m = 100$ and $m = 200$ provide an excellent trade-off between accuracy and data requirements manifesting in a relative peak error of approx. 1.34 and 0.029, respectively, and L2 error of magnitude 10^{-6} in both cases. By choosing an appropriate number of training detunings, BERG can simulate the photon echo experiment with an error that may be tuned further with step size.

B. Convergence with QE size

The second simulation investigates the convergence of the photon echo with the number of QD in the QE. This number N is in reality very large, which incurs high costs for conducting detailed simulations for all QDs. By learning a Koopman model from a subset of trajectories $m \ll N$ trajectories, we can yield a great advantage in efficiency compared to the conventional expensive and time-intensive model.

We fix $N = 10^4$ and $\Delta t = 0.01$. We compare the relative peak error of the Koopman model trained on $m \ll N$ detunings, evaluated on N detunings with the relative peak

error of a reference calculation of N detunings. Since the revival time approaches zero for decreasing number m of QD in the simulated QE, i.e. $T_{rev} \rightarrow 0$ for $(m-1) \rightarrow 0$, the non-physical revival distorts the training data. By tuning the parameters such that T_{rev} exceeds our evaluation time $t = 100$ even for small m , the problem can be circumvented. The resulting parameters are $R = 1$, FWHM = 1 meV and a pulse as shown in Fig. 2. Fig. 8 shows the difference between the polarization trajectory calculated by BERG for different m and the reference trajectory. An error visualization can be found in Fig. 9. We examine that the trajectories of the L2 error and the relative peak error of BERG are similar to the error data in the photon echo experiment, Fig. 7. While the x-axis changed, as now the number of trained detunings m ranges up to $N = 10^4$, we observe a similar, significant dip in the errors. The optimal number of training detunings are $m = 10$ and $m = 50$ with a relative peak error of approx. 0.027 and 0.025, respectively, and L2 error of magnitude 10^{-5} , implying that we have reduced the number of expensive simulations by a factor of 100 with BERG.

V. CONCLUSIONS

We have investigated the possibility of using Koopman operator-based surrogate models to accelerate the analysis of optical quantum systems. Even though the original system has bilinear dynamics, the small inaccuracies of the discrete-time bilinear Koopman model pose significant challenges for long-term predictions such that special care has to be taken during modeling. By introducing a refined training grid for the detuning, stabilization of the model can be achieved, leading to accurate predictions of TLS in an RWA. Several aspects of training the bilinear model may still be investigated. For example, the effect of other sampling techniques for the detuning control instances has yet to be determined, in distinction to the linearly spaced detunings we applied. In addition, a refined grid for the optical pulse may reduce errors further. The increasing interest in quantum systems will require further research for efficient simulation and control. We demonstrated the potential of a Koopman operator-based model in quantum applications by presenting accuracy results on a simple quantum system. However, further investigation is needed to explore the applicability of this model to more complex quantum systems. Examples include the nonlinear optical dynamics of electronic many-body systems or the ultrafast dynamics of matter driven with extremely strong fields, providing access to attosecond time scales.

VI. ACKNOWLEDGMENTS

AH and SP acknowledge support by the German Federal Ministry of Education and Research (BMBF) within the AI junior research group “Multicriteria Machine Learning”. TM and HR acknowledge funding by the Ministry of Culture and Science of the State of North Rhine-Westphalia via the project PhoQC.

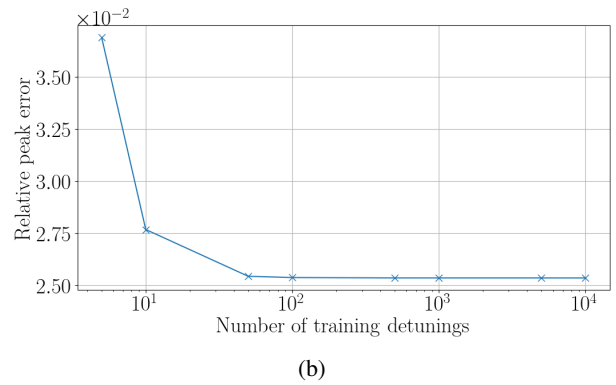
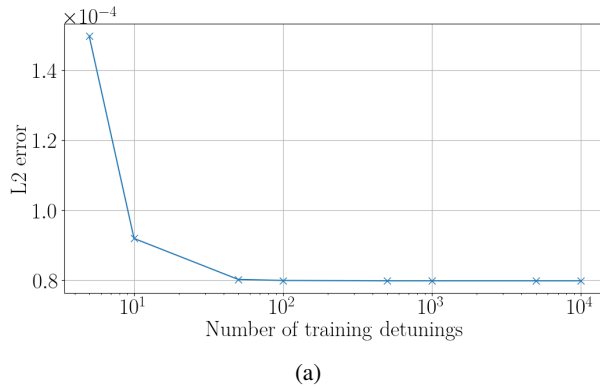


Fig. 9: (a) L2 error and (b) relative peak error for BERG in the convergence simulation. In both cases, $m + 1$ detunings were trained, where $m \in \{5, 10, 50, 100, 500, 1000, 5000, 10000\}$.

REFERENCES

- [1] C. W. ROWLEY, I. MEZIĆ, S. BAGHERI, P. SCHLATTER, and D. S. HENNINGSON, "Spectral analysis of nonlinear flows," *Journal of Fluid Mechanics*, vol. 641, p. 115–127, 2009.
- [2] A. Navarra, J. Tribbia, and S. Klus, "Estimation of koopman transfer operators for the equatorial pacific sst," *Journal of the Atmospheric Sciences*, vol. 78, no. 4, pp. 1227 – 1244, 2021.
- [3] D. Bruder, C. D. Remy, and R. Vasudevan, "Nonlinear system identification of soft robot dynamics using koopman operator theory," in *2019 International Conference on Robotics and Automation (ICRA)*, 2019, pp. 6244–6250.
- [4] B. O. Koopman, "Hamiltonian systems and transformation in hilbert space," *Proceedings of the National Academy of Sciences of the United States of America*, vol. 17, no. 5, pp. 315–318, may 1931.
- [5] I. Mezic, "Spectral properties of dynamical systems, model reduction and decompositions," *Nonlinear Dynamics*, vol. 41, pp. 309–325, 08 2005.
- [6] —, "Analysis of fluid flows via spectral properties of the koopman operator," *Annual Review of Fluid Mechanics*, vol. 45, pp. 357–378, 01 2013.
- [7] P. Schmid, K. E. Meyer, and O. Pust, "Dynamic mode decomposition and proper orthogonal decomposition of flow in a lid-driven cylindrical cavity," 08 2009.
- [8] P. Schmid and J. Sesterhenn, "Dynamic mode decomposition of numerical and experimental data," *Journal of Fluid Mechanics*, vol. 656, pp. 5–28, jul 2010.
- [9] C. Rowley, I. Mezic, S. BAGHERI, P. Schlatter, and D. HENNINGSON, "Spectral analysis of nonlinear flows," *Journal of Fluid Mechanics*, vol. 641, pp. 115 – 127, 12 2009.
- [10] J. H. Tu, C. W. Rowley, D. M. Luchtenburg, S. L. Brunton, and J. N. Kutz, "On dynamic mode decomposition: Theory and applications," *Journal of Computational Dynamics*, vol. 1, no. 2, pp. 391–421, 2014.
- [11] M. O. Williams, I. G. Kevrekidis, and C. W. Rowley, "A data-driven approximation of the koopman operator: Extending dynamic mode decomposition," *Journal of Nonlinear Science*, vol. 25, pp. 1307–1346, jun 2015.
- [12] M. O. Williams, M. S. Hemati, S. T. M. Dawson, I. G. Kevrekidis, I. G. Kevrekidis, and C. W. Rowley, "Extending data-driven koopman analysis to actuated systems," *IFAC-PapersOnLine*, vol. 49, no. 18, pp. 704–709, dec 2016.
- [13] S. L. Brunton, M. Budišić, E. Kaiser, and J. N. Kutz, "Modern koopman theory for dynamical systems," *SIAM Review*, vol. 64, no. 2, pp. 229–340, may 2022.
- [14] S. E. Otto and C. W. Rowley, "Koopman operators for estimation and control of dynamical systems," *Annual Review of Control, Robotics, and Autonomous Systems*, vol. 4, no. 1, pp. 59–87, May 2021.
- [15] A. Mauroy, I. Mezic, and Y. Susuki, *The Koopman Operator in Systems and Control Concepts, Methodologies, and Applications: Concepts, Methodologies, and Applications*. Springer, 2020.
- [16] S. Klus, F. Nüske, and S. Peitz, "Koopman analysis of quantum systems," *Journal of Physics A: Mathematical and Theoretical*, vol. 55, no. 31, p. 314002, jul 2022.
- [17] I. Mezić, "A transfer operator approach to relativistic quantum wavefunction," *Journal of Physics A: Mathematical and Theoretical*, vol. 56, no. 9, p. 094001, feb 2023.
- [18] L. Allen and J. Eberly, *Optical Resonance and Two-level Atoms*. Wiley, New York, 1975.
- [19] T. Meier, P. Thomas, and S. Koch, *Coherent Semiconductor Optics: From Basic Concepts to Nanostructure Applications*. Springer, New York, 2006.
- [20] V. Damon, M. Bonarota, A. Louchet-Chauvet, T. Chanelière, and J.-L. L. Gouët, "Revival of silenced echo and quantum memory for light," *New Journal of Physics*, vol. 13, no. 9, p. 093031, sep 2011.
- [21] A. N. Kosarev, H. Rose, S. V. Poltavtsev, M. Reichelt, C. Schneider, M. Kamp, S. Höfling, M. Bayer, T. Meier, and I. A. Akimov, "Accurate photon echo timing by optical freezing of exciton dephasing and rephasing in quantum dots," *Communications Physics*, vol. 3, dec 2020.
- [22] S. Grisard, A. V. Trifonov, H. Rose, R. Reichardt, M. Reichelt, C. Schneider, M. Kamp, S. Höfling, M. Bayer, T. Meier, and I. A. Akimov, "Temporal sorting of optical multiwave-mixing processes in semiconductor quantum dots," *ACS Photonics*, vol. 10, no. 9, pp. 3161–3170, 2023.
- [23] B. Farkas and H. Kreidler, "Towards a koopman theory for dynamical systems on completely regular spaces," *Phil. Trans. R. Soc. A*, vol. 378, no. 2185, 11 2020.
- [24] S. Klus, F. Nüske, S. Peitz, J.-H. Niemann, C. Clementi, and C. Schütte, "Data-driven approximation of the Koopman generator: Model reduction, system identification, and control," *Physica D: Nonlinear Phenomena*, vol. 406, p. 132416, 2020.
- [25] S. Peitz, S. E. Otto, and C. W. Rowley, "Data-driven model predictive control using interpolated koopman generators," *SIAM Journal on Applied Dynamical Systems*, vol. 19, no. 3, pp. 2162–2193, sep 2020.
- [26] J. L. Proctor, S. L. Brunton, and J. N. Kutz, "Dynamic mode decomposition with control," *SIAM Journal on Applied Dynamical Systems*, vol. 15, no. 1, pp. 142–161, jan 2016.
- [27] P. Virtanen, R. Gommers, T. E. Oliphant, M. Haberland, T. Reddy, D. Cournapeau, E. Burovski, P. Peterson, W. Weckesser, J. Bright, S. J. van der Walt, M. Brett, J. Wilson, K. J. Millman, N. Mayorov, A. R. J. Nelson, E. Jones, R. Kern, E. Larson, C. J. Carey, Í. Polat, Y. Feng, E. W. Moore, J. VanderPlas, D. Laxalde, J. Perktold, R. Cimrman, I. Henriksen, E. A. Quintero, C. R. Harris, A. M. Archibald, A. H. Ribeiro, F. Pedregosa, P. van Mulbregt, and SciPy 1.0 Contributors, "SciPy 1.0: Fundamental Algorithms for Scientific Computing in Python," *Nature Methods*, vol. 17, pp. 261–272, Feb 2020.